

Design of acoustofluidic device for localized trapping

Cite as: Biomicrofluidics 14, 034107 (2020); doi: 10.1063/5.0006649

Submitted: 4 March 2020 · Accepted: 11 May 2020 ·

Published Online: 21 May 2020



View Online



Export Citation



CrossMark

Li-qiang Li,¹ Kun Jia,^{2,a)} Er-yong Wu,¹ Yong-jian Zhu,³ and Ke-ji Yang¹

AFFILIATIONS

¹State Key Laboratory of Fluid Power and Mechatronic Systems, School of Mechanical Engineering, Zhejiang University, No. 38 Zheda Road, Hangzhou 310027, People's Republic of China

²State Key Laboratory for Strength and Vibration of Mechanical Structures, School of Aerospace, Xi'an Jiaotong University, No. 28 West Xianning Road, 710049 Xi'an, People's Republic of China

³Department of Neurosurgery, Second Affiliated Hospital of Zhejiang University School of Medicine, Hangzhou 310009, China

^{a)}Author to whom correspondence should be addressed: kunjia@mail.xjtu.edu.cn

ABSTRACT

State of the art acoustofluidics typically treat micro-particles in a multi-wavelength range due to the scale limitations of the established ultrasound field. Here, we report a spatial selective acoustofluidic device that allows trapping micro-particles and cells in a wavelength scale. A pair of interdigital transducers with a concentric-arc shape is used to compress the beam width, while pulsed actuation is adopted to localize the acoustic radiation force in the wave propagating direction. Unlike the traditional usage of geometrical focus, the proposed device is designed by properly superposing the convergent section of two focused surface acoustic waves. We successfully demonstrate a single-column alignment of 15-μm polystyrene particles and double-column alignment of 8-μm T cells in a wavelength scale. Through proof-of-concept experiments, the proposed acoustofluidic device shows potential applications in on-chip biological and chemical analyses, where localized handing is required.

Published under license by AIP Publishing. <https://doi.org/10.1063/5.0006649>

I. INTRODUCTION

Non-contact immobilization of macromolecules, cells, and other bioparticles plays an important role in life science, biomedicine, and clinical diagnostics.¹ Further enriching the sample density or forming an ordered arrangement within a certain region of the dilute suspension may facilitate the related operations, such as microscopy observation, chemical synthesis, and bio-analytical detection.^{2–5} Using microfluidic systems to handle micro-particles has thrived over the past few decades. In particular, the combination of microfluidics and ultrasound, namely, acoustofluidics, has attracted significant interest because of the label-free manner, fewer target limits (regardless of the electric, magnetic, and optical properties), and high bio-compatibility.⁶ The nonlinear effects of an ultrasonic wave exert the acoustic radiation force (ARF) on the immersed objects. Following the well-established ARF theory, diverse applications using bulk or surface waves have been developed, including aggregation, separation, and transportation.^{7–11} Theoretical and experimental studies have revealed that ARF depends

on the time-averaged energy density ($\varepsilon = \rho_0 \tilde{v}^2/2 + \tilde{p}^2/(2\rho_0 c^2)$, where \tilde{v} and \tilde{p} are the time-averaged velocity and acoustic pressure, respectively, and ρ_0 and c are the density and sound speed of the medium). To radiate sufficient energy, the employed ultrasonic transducers are difficult to be minimized in the wavelength scale. The established acoustic field occupies a wide range of the fluidic channel, with at least several wavelengths in the direction perpendicular to the wave vector. The generated ARF is imposed on massive targets. However, in bio-research, the intercellular communication and stochastic behavior of cells at a population level induce the exhibition of biologically heterogeneous phenotypes,¹² which lowers the analysis accuracy and definiteness. Correspondingly, localized trapping is anticipated. Another example is developing new therapeutic agents via drug-cell interactions. The employed liposome containing drugs needs to be precisely trapped and ripped at the assigned area.¹³

Focused beam, which has been successfully applied in medical scanning and non-destructive testing, has been adopted to improve the spatial selectivity of trapping in a large volume.^{14–17} For a certain focal length, the arc length of the concave transducer

cannot be too small to achieve a satisfying beam compression ratio. Besides tuning the wavefront, localized trapping is achieved by controlling the phase and amplitude of multiple transducers.^{18–21} Bernassau *et al.* proposed a heptagonal cavity equipped with seven lead-zirconate-titanate transducers to trap microspheres at the desired position.¹⁸ By using nine transducers and the sound field synthesis technique, our previous study showed the rotation of a single silica rod.²¹ Considering the inherent properties of a bulk wave transducer (concave surface and large volume), application of the above localization strategies to microfluidics remains challenging.

The intrinsic chip-integrated characteristics of a surface acoustic wave (SAW) make it an ideal acoustic source for lab-on-chip devices.⁶ A SAW can be conveniently excited by an interdigital transducer (IDT) deposited on a piezoelectric substrate. One- or two-dimensional trapping of bio-particles or cells was successfully achieved in acoustofluidics with straight IDTs, while refinement and localization of the trapping pattern by employing higher frequency or other methods still thrive.^{22–24} David *et al.* adopted pulsed actuation of two IDTs to confine the scale of equilibriums in several wavelengths along the wave propagation direction.²⁴ By modifying the straight electrode to a circular shape, a focused SAW is generated. Taking advantage of the high-power intensity and large compression ratio, enhanced droplet translocations and mixing are demonstrated on a substrate patterned with a focused interdigital transducer (FIDT).^{25–27} Recently, a pair of FIDTs was employed in a cell sorter to improve the operating resolution,²⁸ where the geometrical focuses of the FIDTs were designed to overlap. The width of the established trapping region could be minimized to 160 μm , which is slightly larger than the wavelength (100 μm), but more than ten trapping locations exist in the beam axis. It should be notified that an FIDT cannot converge the energy at the geometrical focus as a bulk wave transducer. SAW-based manipulations result from the coupling between the fluid and oscillating substrate surface. The traveling SAW leaks into the fluid layer, forming a longitudinal pressure wave with an incident angle, called the Rayleigh angle. Hence, the convergent field generated by FIDT is related to not only the electrode's shape but also the mechanical properties of the substrate. When FIDTs are fabricated on a piezoelectric substrate, the effects of material anisotropy on SAW propagation should be considered.

The present work reports a spatial selective acoustofluidic device to trap micro-particles within a wavelength region (both in the wave propagating axis and the orthogonal direction). Pulsed excitation of two FIDTs on a lithium niobate (LN) plate is employed to establish a localized ARF field. The detailed design parameters, including the relative location of FIDTs and micro-channel width, are analyzed. Finally, localized trapping of micro-particles and cells is performed as a proof-of-concept demonstration of our prototype device. The further application studies may provide a contactless handling technique for on-chip analyses requiring high spatial resolution.

II. FOCUSED SAW

SAW-based actuators and sensors work at several tens of megahertz to gigahertz. LN, a man-made single crystal with a

trigonal system, is widely used as the substrate to diminish the attenuation of high-frequency ultrasonic waves. By using this material, elastic anisotropy is inherent in the features of piezoelectricity. The effects of material anisotropy on wave propagation have been known for a long time. The ratio between the stiffness constants c_{44} and c_{55} of 128°-rotated Y-cut X-propagating LN is up to 1.330.²⁹ Accordingly, the velocity variation of SAW in different directions is non-negligible.

For LN excited by an FIDT, the focusing behavior is more complicated than that of a focused beam in fluid. The convergent field results from the superposition of SAW modes at different propagation angles. Previous analysis based on the angular spectrum theory revealed that the acoustic energy generated by a circular-arc IDT is not focused on a single point but onto a narrow beam along the propagating axis.^{30,31} The long beam starts behind the geometric focal point. For highly focused IDTs ($>30^\circ$), the exact focal region is difficult to be analytically derived because of the diffraction-limited beam size. Here, finite element analysis is performed in COMSOL Multiphysics to identify the convergence of SAW on a LN substrate.

The employed FIDT [Fig. 1(a)] has the concentric circular-arc shape to overcome the deteriorated convergence of multiple finger pairs. The geometric focal point is marked by point "A." Eight pairs of electrodes are included. Following are the design parameters: angle $\theta = 60^\circ$, geometric focal length $F_g = 6.3$ mm, and electrode with 75- μm width and interval. The substrate with 20 mm length, 9-mm width, and 300- μm thickness is fixed at the bottom. To suppress the reflected waves, a low-reflection boundary is applied to the substrate's peripheries. The electrical-mechanical coupling is taken into account by introducing a piezoelectric constitutive model. The adopted material parameters are listed in Eqs. (S1)–(S3) in the [supplementary material](#), corresponding to the 128°-rotated Y-cut X-propagating LN. The x- and y-axes of the coordinate system correspond to the x- and y-crystal-axes, respectively. The center of the first electrode is selected as the origin, and the distance from the origin to the geometrical focus is 6.3 mm. The FIDT is modeled as a massless conductor because of its small thickness (200 nm), and a 10V_{pp} voltage is imposed for actuation. Due to the large computational requirement of a three-dimensional model, only half of the entire structure is built and the plane of symmetry plane is along the x-axis.

The maximum amplitude of the Rayleigh wave is achieved when the width and interval distance of the electrode equal a quarter wavelength. To derive the operating frequency, eigenfrequency analysis is firstly performed on the LN substrate with periodic IDTs (see Fig. S1 in the [supplementary material](#)). Only the mode with 12.65-MHz resonant frequency corresponds to a 300- μm wavelength. Hence, 12.65 MHz is selected as the excitation frequency in the following frequency response analysis. The mesh accuracy is ascertained through a mesh refinement study (see Fig. S2 in the [supplementary material](#)).

The total displacement is shown in Fig. 1(b). In the near-field, two curves with high intensity appear, which are usually referred to caustics in ray acoustics. Between the caustics, there are interference patterns. In the far field, the energy is confined to a narrow region named as physical focal spot, but sidelobes appeared on the upper and lower sides. To validate the numerical prediction, SAW on the

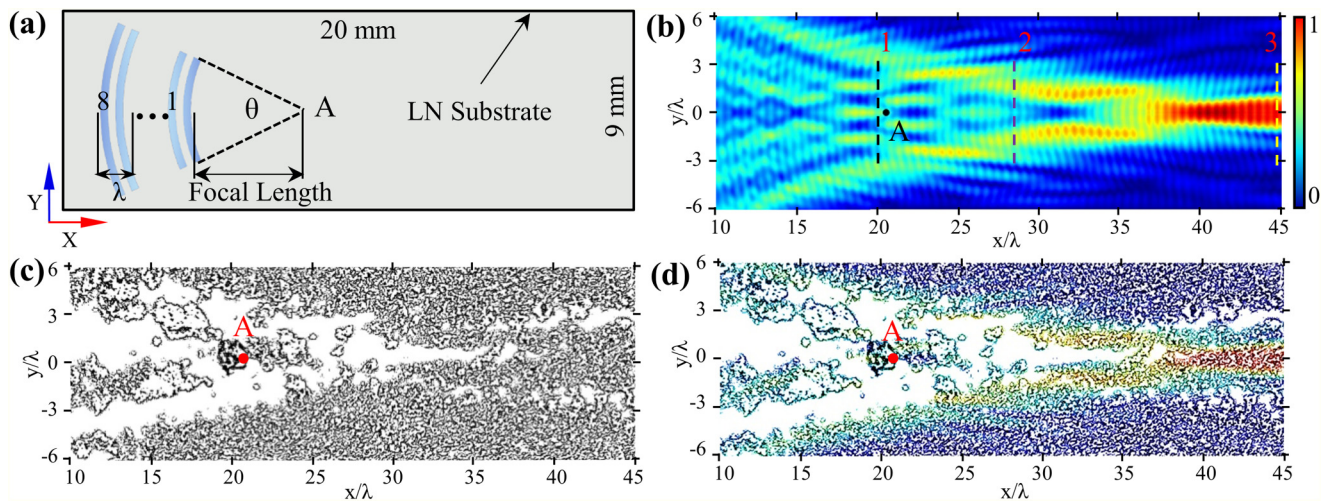


FIG. 1. (a) Geometric model used in the finite element analysis. (b) Calculation of the normalized displacement on the LN surface when FIDT is continuously actuated by a 12.65-MHz sinusoidal signal. Point "A" represents the geometric focal point. (c) Redistribution of 5- μm silicon dioxide microparticles for visualization of SAW convergence. (d) The predicted SAW profile corresponds well with the redistribution of microparticles.

LN surface was visualized. According to the method proposed by Tan *et al.*,³² the dispersed smoke particles on the LN substrate redistributed due to the effects of substrate oscillation and acoustic streaming. Here, silicon dioxide microparticles (about 5 μm in diameter) were sprayed on the LN substrate (details of the fabrication are given in Sec. III). When the FIDT was actuated by a 12.8-MHz sinusoidal signal with 30V_{pp} (28-dBm, the actual resonant frequency slightly differs from the calculation; see Fig. S3 in the supplementary material), the micro-particles redistributed and outlined the focused SAW. The white areas in Fig. 1(c) correspond to the places where no residuals, so more light comes into the view. And the black areas demonstrate the agglomerations. According to the previous studies,³³ micro-beads were collected at the antinodes corresponding to larger vibration displacement. Since 5- μm microbeads were employed here, we suppose that silicon dioxide micro-particles move toward to the region with larger SAW amplitudes, which approximates the actual focus. By superimposing the

numerical prediction Fig. 1(b) and the measurement Fig. 1(c), the calculated profile corresponds well with the particle distribution pattern [Fig. 1(d)]. The white bifurcation (no residual particles) in the range between 35- and 45-lambda happens to be distributed on the upper and lower sides of the physical focal point. In the following design, the numerically predicted SAW profiles will be used.

III. DEVICE DESIGN AND FABRICATION

A. Prototype device

The proposed device, as shown in Fig. 2, comprises a LN substrate, a polydimethylsiloxane (PDMS) channel, and a pair of metallic FIDTs. The double-side-polished 128°-rotated Y-cut X-propagating LN substrate with a thickness of 0.5 mm was used due to its high coupling coefficient ($K_2 = 5.3\%$).³⁴ Aluminum FIDTs with a thickness of 200 nm were fabricated on the LN surface by standard photolithography, magnetron sputtering, and

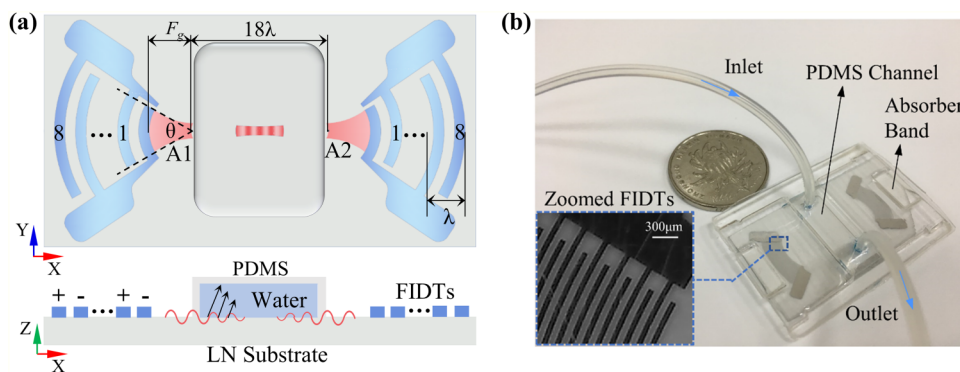


FIG. 2. (a) Schematic of the proposed acoustofluidic device. (b) Prototype device showing the FIDTs, inlet, outlet, absorber band, and PDMS channel. The FIDT is magnified on the lower-left panel.

life-off process.³⁵ Each FIDT has eight pairs of concentric circular-arc electrodes, while the other parameters are the same as those used in Sec. I (i.e., $\theta = 60^\circ$, $F_g = 6.3$ mm, $\lambda = 300 \mu\text{m}$). The distance between the geometric focal points of two FIDTs was set as $5400 \mu\text{m}$ (18λ). A polydimethylsiloxane (PDMS) channel with a width of 4.8 mm and an inner height of $100 \mu\text{m}$ was fabricated via the mold-replica technique. First, an ABS mold with a negative shape of the PDMS channel was formed by 3D printing (Objet350, Stratasys, USA). Then, the silicone elastomer precursor (DC184, DOW CORNING, USA) and a curing agent were mixed with a weight ratio of 10:1 and injected into the plastic mold. The PDMS was cured at 65°C after degassing and treated with plasma (3 min) before bonding to the LN surface. Sockets embedded in a printed circuit board (PCB) were connected to the FIDT pads using silver conductive epoxy. Finally, the edges of the LN substrate were covered with an acoustic absorber (also formed of PDMS) to prevent the reflection of SAWs.

B. Relative location of the FIDTs

When the viscosity of the fluid can be neglected, the ARF resulting from a standing wave field is much stronger than that induced in a traveling wave field. The major task of device design is the establishment of a localized standing wave field by using counter-propagating focused SAWs. Considering the sidelobes near the physical spot, superposition of that section may not satisfy the requirement. Figures 3(a)–3(c) show the calculated total displacement on the LN surface for various distances [0 mm, $5.4 \mu\text{m}$, and $14.4 \mu\text{m}$, the symmetric center corresponds to the dashed lines “1”–“3” marked in Fig. 1(b), respectively] between the geometric focuses of FIDTs. By superposing SAWs around the geometric focal point [Fig. 3(a)], the generated field will be highly interfered, not the required one-dimensional narrow beam. The interference pattern shown in Fig. 3(c), which is derived by superposing the physical focal spot, seems to possess a narrower beam. However, sidelobes appeared on the upper and lower sides of physical focus may broaden the trapping in the y-axis. Meanwhile, the superposed wave field is far from the traditional standing wave, and the influence of the traveling wave component may not be ignored since the

ARF in the traveling wave is much smaller than that in the standing wave. In Figs. 4(a)–4(c), the phase variations [along lines “h” and “i” marked in Figs. 3(a)–3(c)] reveal the fact that localized standing wave field is only achieved when the superposed field locates ahead of the focus. In the center of the LN substrate, the standing wave components (the phase change of π every half wavelength) extend to a wider range ($>800 \mu\text{m}$) for the fields built with geometric and physical focal spots. The corresponding trapping pattern may occupy a wider range in the y-axis. For the superposed field in Fig. 3(b), the traveling wave component (linear phase change from π to $-\pi$ every wavelength) dominates when the y-axis exceeds $400 \mu\text{m}$ [Fig. 4(b)]. It is also worth noting that the y-axis amplitude gradient points to the beam axis in Fig. 3(b) while reverses in Fig. 3(c). The effects of generated y-axis ARF will push the trapped particles around the beam axis.

According to the above analysis, the counter-propagating focused SAWs should be overlapped at the section ahead of the physical focal spot [Fig. 3(b)] to confine the region of the generated standing wave. The proper distance between the geometric focuses of FIDTs should be within 4.2–5.4 mm.

C. Width of the microchannel

The functionality of SAW-based microfluidics depends on the acoustic field in the water-contained microchannel above the substrate. Thus, we further analyze the influence of fluid width on the leaky wave. A fluid domain is added to the LN surface, and the numerical model includes acoustic-structure interactions. The length and height are fixed at 3.6 mm and $100 \mu\text{m}$, respectively. Different widths (16λ , 24λ , and 36λ) along the SAW propagating direction are investigated. The medium is water, with a density of 980 kg/m^3 and a sound speed of 1450 m/s . Impedance boundaries are applied to the fluid, modeling the acoustic effects of the PDMS channel (density $\rho = 920 \text{ kg/m}^3$ and sound speed $c = 1076.5 \text{ m/s}$).

The calculated acoustic intensity on the x-y cross section with a height of $50 \mu\text{m}$ is shown in Figs. 5(a)–5(c). For the channel with lengths of 24λ and 36λ , the waves could not converge into a high-intensity beam due to the propagation attenuation. When the SAW travels along the LN-fluid interface, acoustic energy is continuously

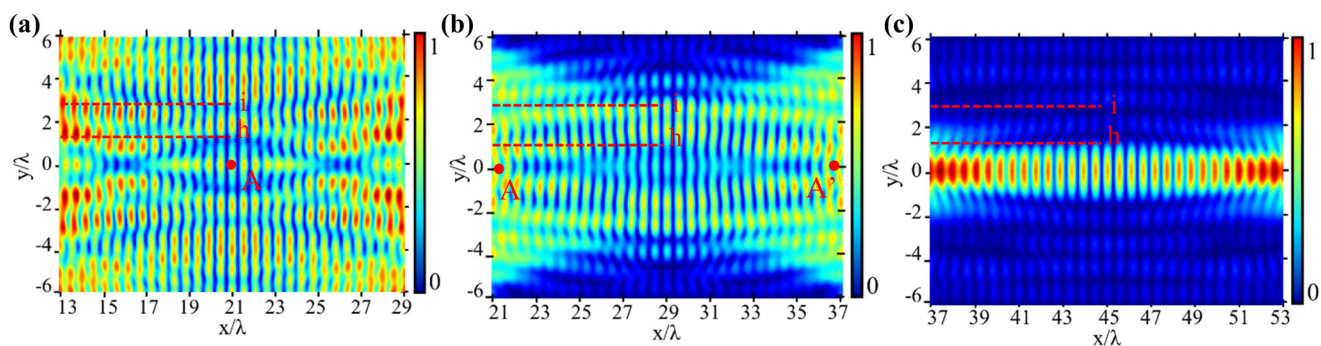


FIG. 3. (a)–(c) Normalized displacement on the LN surface calculated by superposing two counterpropagating focused SAWs. The dashed lines marked in Fig. 1(b) are selected as the centerlines of two geometric focuses, respectively.

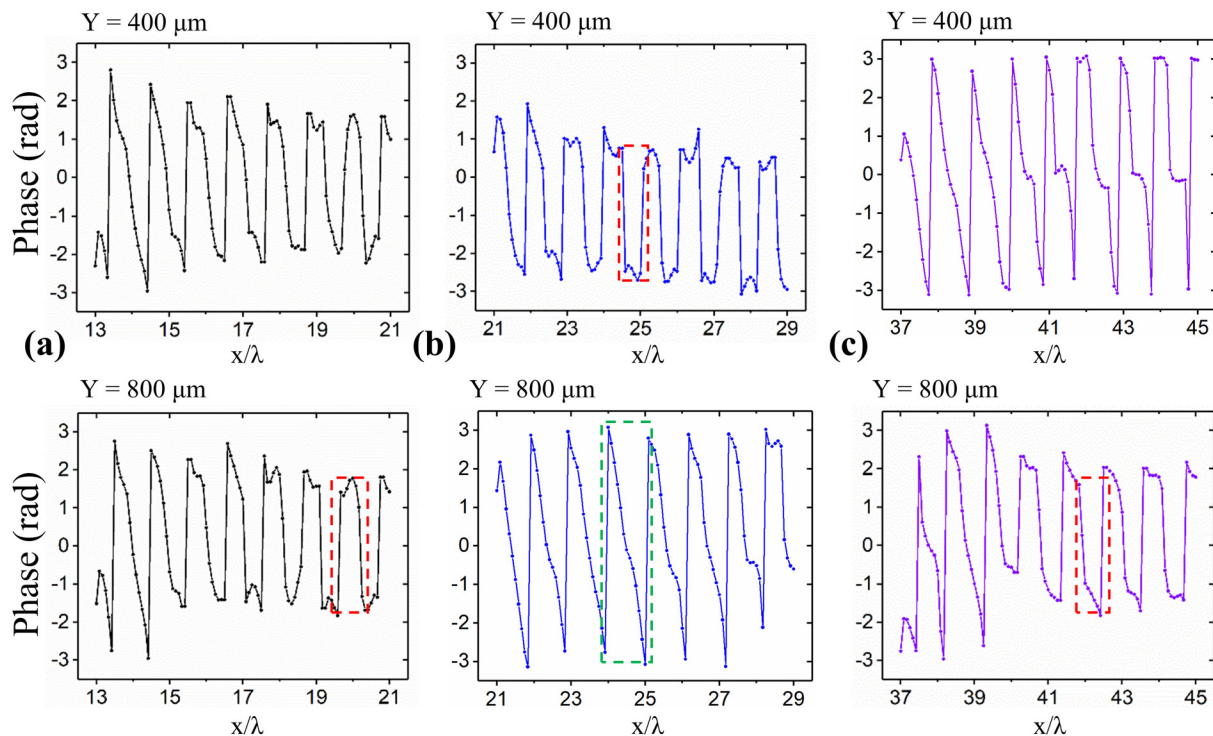


FIG. 4. (a)–(c) Phase variations along lines “h” and “i” marked in Figs. 3(a)–3(c). The phase of a traveling wave component (marked by a dashed green box) linearly changes from π to $-\pi$ along the wave propagating direction, while the phase abruptly changes π every half wavelength for a standing wave (marked by a dashed red box).

emitted into the fluid. The resulting longitudinal wave is attenuated within a few wavelengths depending on the liquid density and substrate material property.³⁶ Hence, the overall length of the PDMS channel needs to be limited for a stronger energy concentration. For our design (16λ -length), the acoustic energy is uniformly distributed in the fluid, and the beam maintains the same pattern at different fluid heights (see Fig. S4 in the [supplementary material](#)).

IV. ARF UNDER PULSED ACTUATION

From the continuous-phase variation as shown in Fig. 4(b), it is clear that the superposition of two focused SAWs contains traveling wave components. The traveling wave may induce a large-scale Eckart streaming, which disturbs the trapped targets.³⁷ Note that the time scale for establishing Eckart streaming is in the order of seconds,^{38,39} so short-time actuation may be employed to suppress the streaming while maintaining the trapping ability of the acoustofluidic device.

Figure 6(a) illustrates the trapping mechanism of pulsed SAWs. The continuous excitation of the FIDT with N pairs of electrodes is changed to a pulse with M cycles of sinusoidal signal. Two SAW pulses are generated and propagate in opposite directions. Figure 6(b) shows the relation of the excitation and SAW pulse, which is evaluated based on the delta-function model of IDT.⁴⁰

Due to the superposing actuation effects of IDT, the SAW amplitude increases through time and reaches a steady state after N wave periods. At the end of the excitation (after M periods), the amplitude begins to decrease. So the width of the SAW pulse is defined as $M + N$. The pulses encounter at the center region of the LN substrate, and a localized interference field is formed in the PDMS channel. With a suitable pulse width and repetitive frequency, only two pulses counter-propagate on the substrate at any time. The existing time ($M + N$ periods) of the acoustic field could be made much shorter than the developing time of acoustic streaming.

Here, we assume $M \leq N$ to make the pulse width as small as possible. Transient analysis is performed with a time step of $\Delta t = 1.3021 \times 10^{-9}$ s, and the related parameters are listed in Table S1 in the [supplementary material](#). For the actuation containing six cycles of 12.65-MHz sinusoidal signal, Figs. 7(a)–7(d) show the transient z-axis displacement on the LN substrate and the leaky wave. Starting from $t = 21T$ ($T = 1/f$), the generated SAWs leak into the fluid and then encounter at $t = 29T$. The counter-propagating waves completely overlap at $t = 36T$ and separate at $t = 43T$. After $t = 51T$, the waves escape from the region covered with fluid, resulting in the evanescence of the acoustic field.

The classical ARF theory derived from the perturbation method treats the force as a time-averaged effect in a wave period. For a transient field, the ARF model⁴¹ should be modified. We

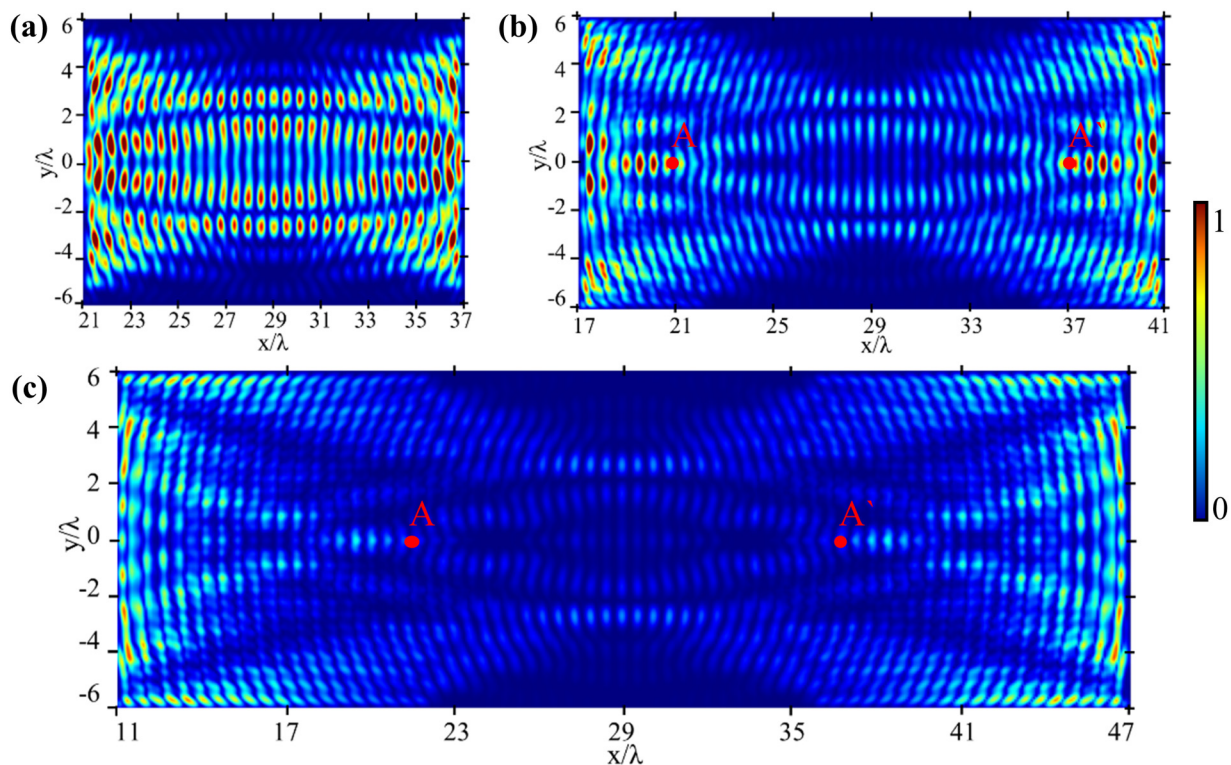


FIG. 5. (a)–(c) Normalized acoustic intensity calculated in the fluid layer at a height of $50\ \mu\text{m}$. The lengths of the microchannel are 16λ , 24λ , and 36λ .

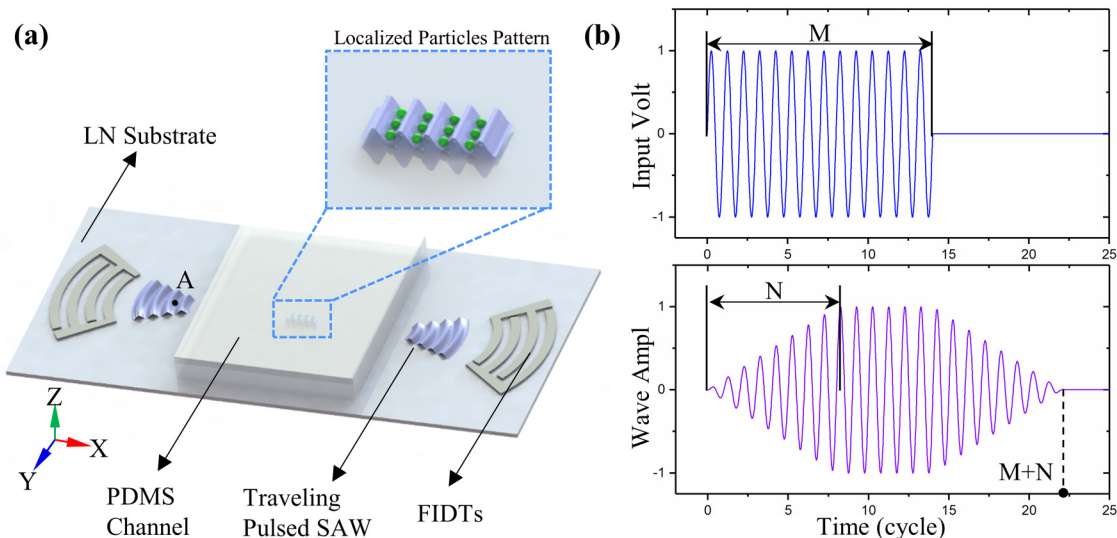


FIG. 6. (a) Working principle of microparticle trapping by using focused SAW pulses. Point "A" is the geometrical focus of the FIDT. When the FIDTs are actuated by the pulsed voltage, two focused SAW pulses are generated, trapping the microparticles within the water-contained PDMS channel. (b) Simulation reveals that $M+N$ cycles of SAW are generated by actuating the N -pair electrode FIDT with M cycles of sinusoidal voltage.

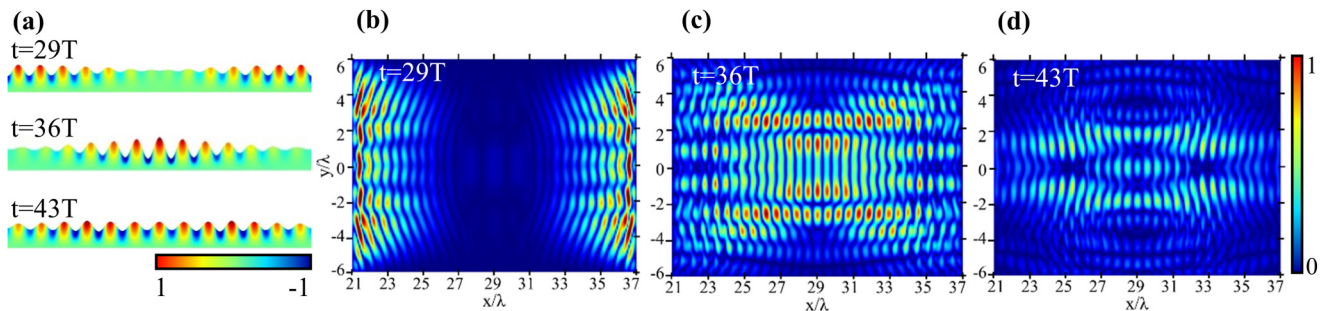


FIG. 7. (a) Calculated z-axis displacement on the LN surface. (b)–(d) Predicted transient acoustic fields in the liquid-contained PDMS channel.

assume that the radiation force F^{rad} of transient acoustic waves can be calculated by extending the average time to T_n , which corresponds to the repetitive frequency of the pulsed wave,

$$\begin{aligned} F^{rad} &= -\pi a^3 \left[\frac{2k_0}{3} \operatorname{Re}[f_1^* p_{avg}] - \rho_0 \operatorname{Re}[f_2^* v_{avg}] \right], \\ p_{avg}(x, y) &= \frac{1}{T_n} \int_0^{T_n} [p_{in}^*(x, y, t) \nabla p_{in}(x, y, t)] dt, \\ v_{avg}(x, y) &= \frac{1}{T_n} \int_0^{T_n} [(v_{in}^*(x, y, t) \cdot \nabla) v_{in}(x, y, t)] dt, \\ f_1 &= 1 - \frac{k_p}{k_0}, f_2 = \frac{2(\rho_p/\rho_0 - 1)}{2\rho_p/\rho_0 + 1}, \end{aligned} \quad (1)$$

where $p_{in}(x, y, t)$ and $v_{in}(x, y, t)$ are the transient pressure and velocity, k_p and k_0 are the compressibility of the particles and water, and ρ_p and ρ_0 are the density of the particles and water, respectively. The asterisk denotes complex conjugation. Thus, the ARF continuously acts on the micro-particles under pulsed excitation.

Figures 8(a) and 8(b) show the averaged pressure field and the corresponding ARF field at the center region where the standing wave dominates. The time-averaged ARF along the x-axis drives the particles to several locations with minimum averaged pressure. Due to the elongated potential minimum, the trapped particles may contact each other, forming a straight line perpendicular to the beam axis.

V. EXPERIMENTS AND DISCUSSION

A. Experimental setup

The acoustofluidic device was mounted on the stage of an inverted microscope (SUNNY XD, China) equipped with a CCD camera. A 12.8-MHz sinusoidal signal generated by a signal generator (33522B, Agilent, USA) was amplified by an RF power amplifier (ZHL-1-2W, Mini-Circuits, USA) and then applied to the FIDTs. The excitation frequency was derived from the impedance analysis (Fig. S3 in the [supplementary material](#)). By using a peristaltic pump (BQ80S, LEAD FLUID, China), the solution with micro-particles or cells were injected into the microchannel. The particle movement was recorded and the videos were later analyzed using ImageJ to extract the trajectory.

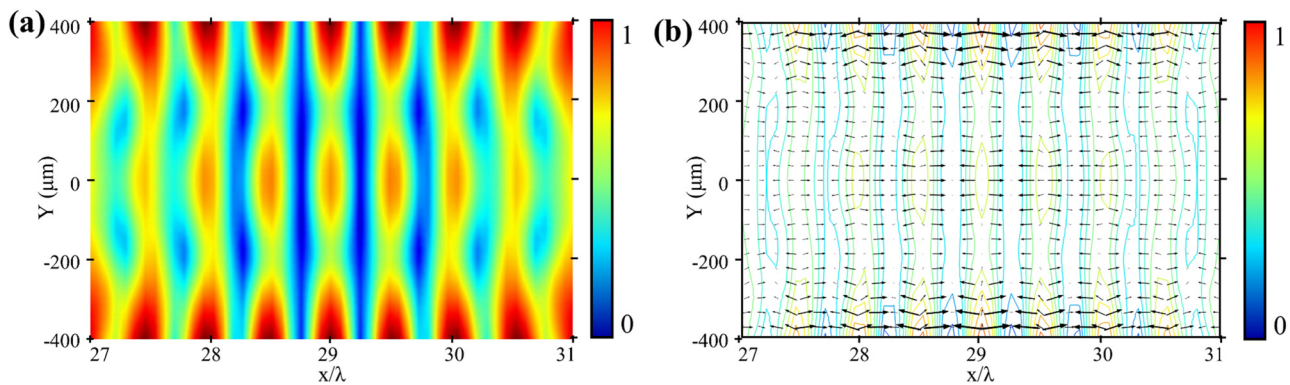


FIG. 8. (a) and (b) Time-averaged pressure field and the corresponding ARF field calculated in the liquid domain.

Monodisperse polystyrene (PS) with diameters of 15 and 1 μm (PS-0010 and PS-0150, RIGOR, China) were diluted in de-ionized water (DI) at a 0.04% weight ratio, respectively. Bioparticles were also prepared. Human peripheral blood mononuclear cells (PBMCs, concentration of 1 million/ml) were cultured in the complete media RPMI-1640 supplemented with 5% human AB serum, 1% penicillin-streptomycin solution, and 300 IU/ml IL-2. Before the experiments, PBMCs were stimulated via anti-CD3/CD28 microbeads for seven days to enrich the T cells. Then, the T cells ($\sim 8 \mu\text{m}$ in diameter) were centrifuged and resuspended in phosphate-buffered saline (PBS) at a concentration of 2 million/ml.

B. Disturbance of continuous excitation

The behavior of 15- μm PS microparticles under $30V_{\text{pp}}$ continuous excitation (28 dBm) shows the effects of acoustic streaming on the manipulation (see Movie S1 in the [supplementary material](#)). The initial particle trajectories are along the x-axis direction and then toward the y-axis. Parallel alignment was achieved only in a narrow beam with a width of about 100 μm . However, the stability of trapped particles is unsatisfactory. Several trapped targets were selected. Then, the particle trajectories were analyzed by ImageJ. [Figure 9\(a\)](#) shows that the particle migration may exceed 75 μm . The initial and final positions of the cluster trajectories are represented by the blue and red dots in [Fig. 9\(b\)](#), respectively. The counter-direction y-axis movement (i.e., clusters 1 and 3 downward and cluster 2 upward) did not result from the ARF along y-axis. Considering the continuous-phase variation of the field [[Fig. 4\(b\)](#)], the traveling wave component induces a large-scale Eckart streaming. As microparticles with small diameters (usually $< 5 \mu\text{m}$) are more easily dominated by acoustic streaming, the solution with 1- μm PS particles was used to visualize the streaming. An apparent flow along the y-axis was established in the scale larger than a wavelength (see Movie S2 in the [supplementary material](#)). In the

beginning, 1- μm PS particles aggregated at the beam center. Due to the unbalanced downward and upward y-axis flows (an asymmetric pattern), the aggregations were driven away from the beam axis. As predicted, the disturbance of Eckart streaming is considerable under continuous excitation.

C. Stable and localized trapping

Finally, trapping PS microparticles was performed under pulsed excitation. The 12.8-MHz sinusoidal voltage was modulated by a 177-kHz pulse width adjustable square wave. The duty cycle of the pulsed signal was set to 0.03, 0.06, 0.09, and 0.12, which makes the pulsed actuation contain two, four, six, and eight cycles of sinusoidal wave, respectively. The excitation parameters ensure the existence of only two pulses on the LN substrate at any time. Under the eight-cycle burst actuation, the 1- μm PS particles moved slowly (see Movie S3 in the [supplementary material](#)) and did not concentrate in the vortex shape. As no apparent flow was observed with $M = 8$, acoustic streaming could be further suppressed by using shorter SAW pulses.

In [Figs. 10\(a\)–10\(d\)](#), 15- μm PS particles form several alignments in the central region marked by the red dashed lines, which are captured at 50 s after excitation. Outside the localized trapping region (indicated by the dashed red line), the ARF is too weak to form alignments. The shorter pulse durations (two and four cycles) could generate fewer alignments (only two) with about 150- μm intervals because particles away from the center move much slower. However, for two-cycle actuation, the y-axis ARF was too weak to agglomerate the microparticles. The preferable single-column self-assembly with more alignments was achieved with six- and eight-cycle actuations. Fluctuations of particles are negligible [[Fig. 10\(e\)](#)].

In fact, the particle alignment is time dependent when the pulsed actuation is employed (see the trapping process of 5- μm PS micro-particles, Fig. S5 and Movie S4 in the [supplementary material](#)).

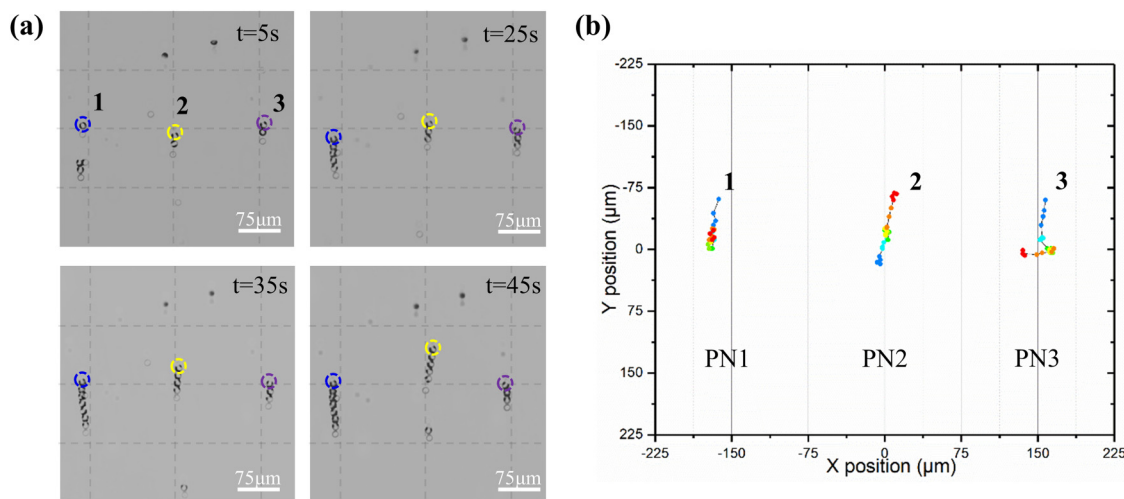


FIG. 9. (a) Migration of 15- μm PS microparticles when the FIDTs are actuated. (b) Particle trajectories. The initial and final positions are represented by blue and red dots, respectively.

The applied excitation contains two cycles of 12.8-MHz sinusoidal signals. It is clear to see that the x-axis trapping region broadens along with time while the y-axis confinement remains constant. As shown in Fig. 8(b), the time-averaged ARF field, especially at the nodal regions, decreases from the middle to both sides along the x-axis. The particles in the center area experience stronger x-axis ARF than those being further from the symmetric center. For the same time interval, particles with larger ARF travel a longer distance. The number of applied sinusoidal signals can be used to tune the variations of x-axis ARF: eight-cycle signal makes smaller variation of the x-axis ARF. Hence, increasing the duty cycle of the

pulsed signal can widen the trapping region in the center of the micro-channel. Similarly, appropriately extending the actuating time of the pulsed excitation may strengthen the alignments and generate a wider trapping region.

For the proposed device, the trapping region is defined by the smallest rectangular enclosing the trapped particles plus half a wavelength, so the x-axis scale will always be an integer. When the pulse width of excitation increases from two cycles to eight cycles, the alignments of PS particles increase from two to six columns [Figs. 10(a)–10(d)]. Accordingly, the region of the alignments in the x-axis extends from a wavelength ($300\text{ }\mu\text{m}$) to two wavelengths

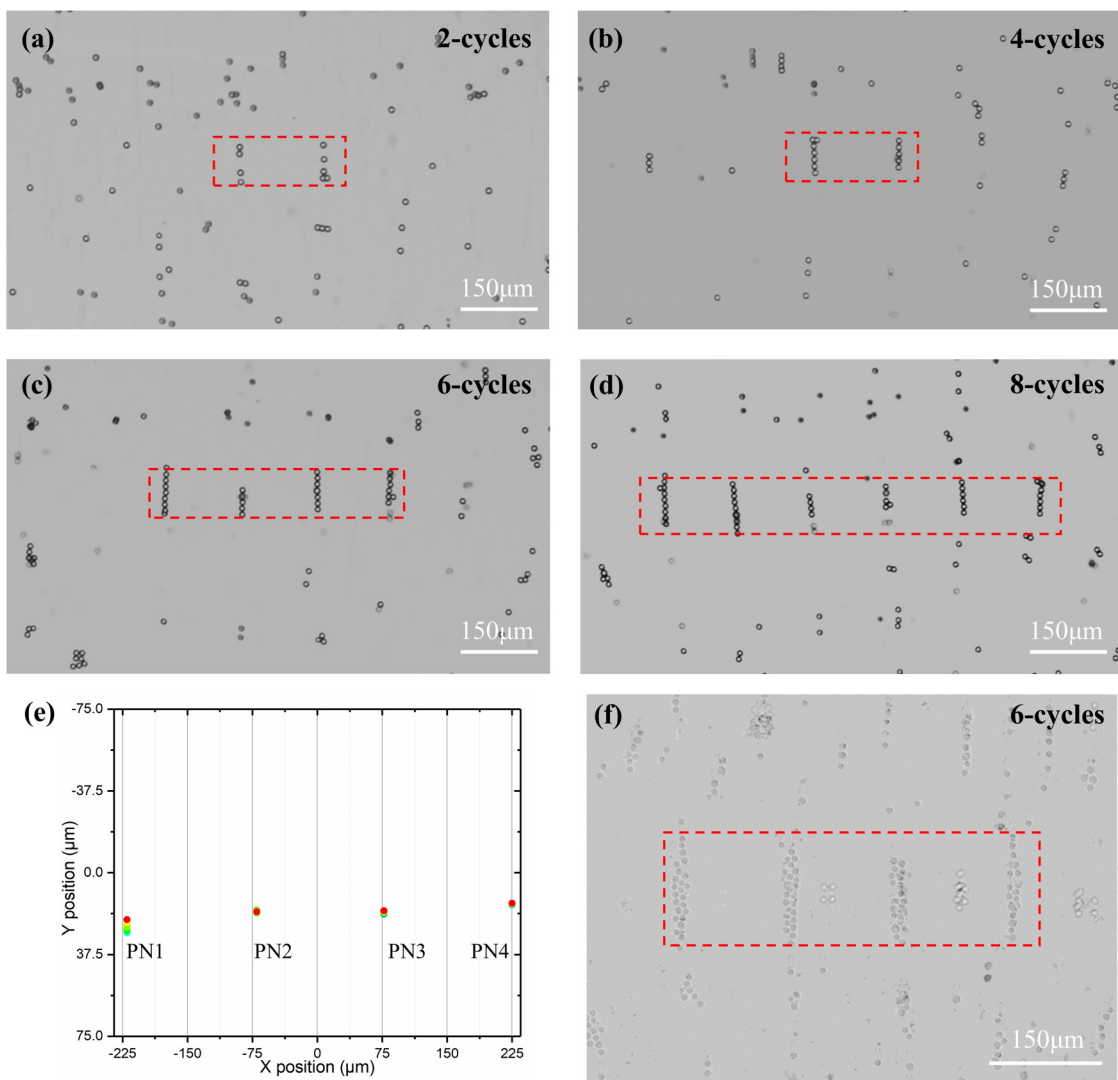


FIG. 10. Stable alignment of $15\text{-}\mu\text{m}$ PS microparticles is realized in a small region when the FIDTs are actuated by $30V_{pp}$ (power of 28 dBm) sinusoidal pulses with 177-kHz repetitive frequency. The applied pulse contains (a) two cycles, (b) four cycles, (c) six cycles, and (d) eight cycles of 12.8-MHz sinusoidal signals. (e) Migration of $15\text{-}\mu\text{m}$ PS clusters shown in (c) after reaching the equilibrium. The initial and final positions are represented by blue and red dots, respectively. (f) Aggregation of T cells ($8\text{ }\mu\text{m}$ in diameter) by using a six-cycle excitation signal.

($600\text{ }\mu\text{m}$), and finally three wavelengths ($900\text{ }\mu\text{m}$). In this process, the trapping region in the y -axis remains the same (about $120\text{ }\mu\text{m}$). Therefore, the smallest capture range in the x -axis is $300\text{ }\mu\text{m}$ [Figs. 10(a) and 10(b)]. The capture range in the y -axis is $160\text{ }\mu\text{m}$ (according to Fig. S5 in the [supplementary material](#)). For comparison, trapping of $5\text{-}\mu\text{m}$ PS micro-particles was also performed within devices designed by superposing the physical focal spots (see Fig. S6 in the [supplementary material](#)). The trapping effects occupy a much larger region in the y -axis ($>1.8\text{ mm}$).

More compressible bioparticles could also be trapped within a small region by the proposed acoustofluidic device. In Fig. 10(f), a slim aggregation of T cells formed at four pressure nodes. For cells with a diameter of $8\text{ }\mu\text{m}$, we find that two columns are established at each equilibrium. Hence, the structure of the particle alignment can be tuned by the size of samples and possibly the wavelength.²³ We will further investigate these issues in our future work.

VI. CONCLUSION

In this study, an acoustofluidic device was presented for ultrasonically trapping microparticles in a specific region with a sub-wavelength scale. To establish the localized ARF field, counter-propagating focused SAW pulses were excited on the LN substrate. Finite element analysis and experiments revealed the convergent beam generated by the 60° FIDT. Accordingly, the acoustofluidic device was configured with a 5.4-mm distance between the geometric focuses of two FIDTs. For a pulsed actuation with no more than eight cycles of sinusoids, a localized single-column alignment of $15\text{-}\mu\text{m}$ PS particles was achieved (within $300 \times 120\text{ }\mu\text{m}$) while $8\text{-}\mu\text{m}$ T cells were aligned in a double column. The employed pulsed excitation also played an important role in suppressing the Eckart streaming accompanied with the focused SAWs. Hence, the trapping stability was much improved compared to the performance under continuous actuation. By tuning the acoustic energy in the form of a pulse duration, the proposed device can assemble sparsely trapped particles in closely connected lines. In addition, the column number of the microparticle alignment was found to be dependent on the size of the samples. Our work offered a way to design FIDT based acoustofluidics by considering the anisotropy of employed piezoelectrics. Through proof-of-concept experiments, the FIDT based device presented in this work has the potential to inspire more sophisticated acoustofluidics for lab-on-chip applications such as the patterning, printing, and sorting of cells.

SUPPLEMENTARY MATERIAL

See the [supplementary material](#) for details on material properties, eigenfrequency analysis, mesh-convergence study, and actual operating frequency of the device. The supplementary movies show recordings of particle movements.

ACKNOWLEDGMENTS

This work is supported by the National Natural Science Foundation of China (Nos. 51675480 and 11872292) and the Natural Science Foundation of Jiangsu (No. BK20181188).

DATA AVAILABILITY

The data that support the findings of this study are available within the article [and its [supplementary material](#)].

REFERENCES

- ¹A. Ozcelik, J. Rufo, F. Guo, Y. Gu, P. Li, J. Lata, and T. J. Huang, "Acoustic tweezers for the life sciences," *Nat. Methods* **15**(12), 1021 (2018).
- ²S. R. Khetani and S. N. Bhatia, "Microscale culture of human liver cells for drug development," *Nat. Biotechnol.* **26**, 120 (2007).
- ³G. T. Van Nhieu, C. Clair, R. Bruzzone, M. Mesnil, P. Sansonetti, and L. Combettes, "Connexin-dependent inter-cellular communication increases invasion and dissemination of shigella in epithelial cells," *Nat. Cell Biol.* **5**(8), 720 (2003).
- ⁴C. Smith, "Tools of the trade," *Nature* **446**, 219 (2007).
- ⁵J. Khandurina and A. Guttman, "Bioanalysis in microfluidic devices," *J. Chromatogr. A* **943**(2), 159 (2002).
- ⁶X. Ding, P. Li, S. C. Lin, Z. S. Stratton, N. Nama, F. Guo, D. Slotcavage, X. Mao, J. Shi, F. Costanzo, and T. J. Huang, "Surface acoustic wave microfluidics," *Lab Chip* **13**(18), 3626 (2013).
- ⁷J. Friend and L. Y. Yeo, "Microscale acoustofluidics: Microfluidics driven via acoustics and ultrasonics," *Rev. Mod. Phys.* **83**(2), 647 (2011).
- ⁸S. Deng, K. Jia, J. Chen, D. Mei, and K. Yang, "Relative position control and coalescence of independent microparticles using ultrasonic waves," *J. Appl. Phys.* **121**(18), 184503 (2017).
- ⁹L. Meng, F. Cai, Z. Zhang, L. Niu, Q. Jin, F. Yan, J. Wu, Z. Wang, and H. Zheng, "Transportation of single cell and microbubbles by phase-shift introduced to standing leaky surface acoustic waves," *Biomicrofluidics* **5**(4), 44104 (2011).
- ¹⁰K. Park, J. Park, J. H. Jung, G. Destgeer, H. Ahmed, and H. J. Sung, "In-droplet microparticle separation using travelling surface acoustic wave," *Biomicrofluidics* **11**(6), 064112 (2017).
- ¹¹G. Simon, M. A. B. Andrade, J. Reboud, J. Marques-Hueso, M. P. Y. Desmulliez, J. M. Cooper, M. O. Riehle, and A. L. Bernassau, "Particle separation by phase modulated surface acoustic waves," *Biomicrofluidics* **11**(5), 054115 (2017).
- ¹²K. F. Zaidi and N. Agrawal, "Microstencil-based spatial immobilization of individual cells for single cell analysis," *Biomicrofluidics* **12**(6), 064104 (2018).
- ¹³L. Meng, Z. Deng, L. Niu, F. Li, F. Yan, J. Wu, F. Cai, and H. Zheng, "A disposable microfluidic device for controlled drug release from thermal-sensitive liposomes by high intensity focused ultrasound," *Theranostics* **5**(11), 1203 (2015).
- ¹⁴J.-L. Thomas, R. Marchiano, and D. Baresch, "Acoustical and optical radiation pressure and the development of single beam acoustical tweezers," *J. Quant. Spectrosc. Radiat. Transfer* **195**, 55 (2017).
- ¹⁵M. A. B. Andrade, N. Pérez, and J. C. Adamowski, "Review of progress in acoustic levitation," *Braz. J. Phys.* **48**(2), 190 (2017).
- ¹⁶C. Lee, J. Seob Jeong, J. Youn Hwang, J. Lee, and K. Kirk Shung, "Non-contact multi-particle annular patterning and manipulation with ultrasound micro-beam," *Appl. Phys. Lett.* **104**(24), 244107 (2014).
- ¹⁷H. A. Hancock, L. H. Smith, J. Cuesta, A. K. Durrani, M. Angstadt, M. L. Palmeri, E. Kimmel, and V. Frenkel, "Investigations into pulsed high-intensity focused ultrasound-enhanced delivery: Preliminary evidence for a novel mechanism," *Ultrasound Med. Biol.* **35**(10), 1722 (2009).
- ¹⁸A. L. Bernassau, P. G. Macpherson, J. Beeley, B. W. Drinkwater, and D. R. Cumming, "Patterning of microspheres and microbubbles in an acoustic tweezers," *Biomed. Microdevices* **15**(2), 289 (2013).
- ¹⁹F. Gesellchen, A. L. Bernassau, T. Dejardin, D. R. Cumming, and M. O. Riehle, "Cell patterning with a heptagon acoustic tweezer—Application in neurite guidance," *Lab Chip* **14**(13), 2266 (2014).
- ²⁰P. Glynne-Jones, C. E. Demore, C. Ye, Y. Qiu, S. Cochran, and M. Hill, "Array-controlled ultrasonic manipulation of particles in planar acoustic

- resonator," *IEEE Trans. Ultrason. Ferroelectr. Freq. Control* **59**(6), 1258 (2012).
- ²¹S. Deng, K. Jia, E. Wu, X. Hu, Z. Fan, and K. Yang, "Controllable micro-particle rotation and transportation using sound field synthesis technique," *Appl. Sci.* **8**(1), 73 (2018).
- ²²J. Shi, D. Ahmed, X. Mao, S. C. Lin, A. Lawit, and T. J. Huang, "Acoustic tweezers: Patterning cells and microparticles using standing surface acoustic waves (SSAW)," *Lab Chip* **9**(20), 2890 (2009).
- ²³D. J. Collins, B. Morahan, J. Garcia-Bustos, C. Doerig, M. Plebanski, and A. Neild, "Two-dimensional single-cell patterning with one cell per well driven by surface acoustic waves," *Nat. Commun.* **6**, 8686 (2015).
- ²⁴D. J. Collins, D. Citsabehsan, Z. Ma, N. J. Wei, N. Adrian, and A. Ye, "Acoustic tweezers via sub-time-of-flight regime surface acoustic waves," *Sci. Adv.* **2**(7), e1600089 (2016).
- ²⁵Y. Ai and B. L. Marrone, "Droplet translocation by focused surface acoustic waves," *Microfluid. Nanofluid.* **13**(5), 715 (2012).
- ²⁶R. Shilton, M. K. Tan, L. Y. Yeo, and J. R. Friend, "Particle concentration and mixing in microdrops driven by focused surface acoustic waves," *J. Appl. Phys.* **104**(1), 014910 (2008).
- ²⁷J. Nam, W. S. Jang, and C. S. Lim, "Micromixing using a conductive liquid-based focused surface acoustic wave (CL-FSAW)," *Sens. Actuators B* **258**, 991 (2018).
- ²⁸L. Ren, Y. Chen, P. Li, Z. Mao, P. H. Huang, J. Rufo, F. Guo, L. Wang, J. P. McCoy, S. J. Levine, and T. J. Huang, "A high-throughput acoustic cell sorter," *Lab Chip* **15**(19), 3870 (2015).
- ²⁹M. K. Tan, J. R. Friend, O. K. Matar, and L. Y. Yeo, "Capillary wave motion excited by high frequency surface acoustic waves," *Phys. Fluids* **22**(11), 112112 (2010).
- ³⁰T.-T. Wu, H.-T. Tang, Y.-Y. Chen, and P.-L. Liu, "Analysis and design of focused interdigital transducers," *IEEE Trans. Ultrason. Ferroelectr. Freq. Control* **52**(8), 1384 (2005).
- ³¹Q. Dong-Hai, W. Cheng-Hao, and W. Zuo-Qing, "Focusing of surface acoustic wave on a piezoelectric crystal," *Chin. Phys. Lett.* **23**(7), 1834 (2006).
- ³²M. K. Tan, J. R. Friend, and L. Y. Yeo, "Direct visualization of surface acoustic waves along substrates using smoke particles," *Appl. Phys. Lett.* **91**(22), 224101 (2007).
- ³³M. Dorrestijn, A. Bietsch, T. Acikalin, A. Raman, M. Hegner, E. Meyer, and C. Gerber, "Chladni figures revisited based on nanomechanics," *Phys. Rev. Lett.* **98**(2), 026102 (2007).
- ³⁴W. Connacher, N. Zhang, A. Huang, J. Mei, S. Zhang, T. Gopesh, and J. Friend, "Micro/nano acoustofluidics: Materials, phenomena, design, devices, and applications," *Lab Chip* **18**(14), 1952 (2018).
- ³⁵A. Fakhfouri, C. Devendran, T. Albrecht, D. J. Collins, A. Winkler, H. Schmidt, and A. Neild, "Surface acoustic wave diffraction driven mechanisms in microfluidic systems," *Lab Chip* **18**(15), 2214 (2018).
- ³⁶M. Alghane, B. X. Chen, Y. Q. Fu, Y. Li, J. K. Luo, and A. J. Walton, "Experimental and numerical investigation of acoustic streaming excited by using a surface acoustic wave device on a 128° YX-LiNbO₃ substrate," *J. Micromech. Microeng.* **21**(1), 015005 (2011).
- ³⁷M. Wiklund, R. Green, and M. Ohlin, "Acoustofluidics 14: Applications of acoustic streaming in microfluidic devices," *Lab Chip* **12**(14), 2438 (2012).
- ³⁸H. Mitome, T. Kozuka, and T. Tuziuti, "Measurement of the establishment process of acoustic streaming using laser Doppler velocimetry," *Ultrasonics* **34**(2), 527 (1996).
- ³⁹K. Jia, K.-j. Yang, and B.-F. Ju, "Performance and robustness improvements in ultrasonic transportation against large-scale streaming," *J. Vib. Acoust.* **138**(2), 021014 (2016).
- ⁴⁰P. J. Feenstra, "Modeling and control of surface acoustic wave motors," Ph.D. thesis (University of Twente, 1978).
- ⁴¹M. Settnes and H. Bruus, "Forces acting on a small particle in an acoustical field in a viscous fluid," *Phys. Rev. E* **85**(1 Pt 2), 016327 (2012).